An efficient and scalable strategy for ultrablack-paint-enabled solar-driven steam generation

Xiaojie Liu [a], Yanpei Tian [a], Fangqi Chen [a], Ralph Ahlgren [b], Yiting Zheng [c], Ming Su [c], Gang Xiao [d], Yi Zheng [a,*]

[a] Department of Mechanical and Industrial Engineering, Northeastern University, Boston, MA 02115, USA
[b] Soleeva Energy, Inc. San Jose, CA 95131, USA
[c] Department of Chemical Engineering, Northeastern University, Boston, MA 02115, USA
[d] Department of Physics, Brown University, Providence, RI 02912, USA

ABSTRACT

Solar-driven interfacial steam generation for desalination has attracted broad attention. However, a significant challenge still remains for achieving a high evaporation rate and high water quality, together with an easy-to-manufacture device to provide a feasible solar-driven steam generation system. In this study, a novel ultrablack paint, Black 3.0, serving as a satisfactory photothermal material is sprayed into the hot-pressed melamine foam networks, allowing us to construct an ultrablack and self-floating evaporation device. The high performing features of effective solar absorption and salt-rejection capability contribute to a high evaporation rate of freshwater at 2.48 kg m^{-2} h^{-1} under one sun (1 kW m^{-2}). This interfacial solar evaporator has a daily drinkable water yield of 2.8 kg m^{-2} even in cloudy winter weather and maintains stability in water with a wide range of acidity and alkalinity (pH 1 ~ 14). All commercially available raw materials and scalable fabrication approaches offer us a feasible and affordable manner to enable the construction of a highly-efficient solar steam generation system for freshwater production.

1. Introduction

Access to freshwater is of pivotal importance to humanity. Fast population growth and climate change demand increasing supply of freshwater. Water scarcity has become a threat to the sustainable development of human society [1,2]. This motivates the development of utilizing saline waters from the oceans and other brackish water sources and the processes that convert saltwater into freshwater. Solar energy is now emerging as one of the most promising sustainable energy sources, as it is clean and can be supplied without any environmental pollution compared with other forms of energy [3]. And the abundant solar energy makes the solar-driven evaporation one of the promising approaches for water desalination and purification [4–6].

In a conventional solar-driven evaporation system, bulk water is heated to a high temperature to generate water vapor, resulting in a slow response to sunlight and heat loss to the bulk water or the external environment [7,8]. Compared with bulk water-heating method which heats the entire body of water, the interfacial solar-driven evaporation approach mainly localizes the heat generation at the air/water interface [9–11]. This method avoids heating a large volume of water, *e.g.,* the ocean, which serves as a low-temperature sink. In 2011, Wang

et al. were among the first to demonstrate the floating interfacial solar-driven evaporation structure into desalination area, which does not require significant capital investment in high-cost permanent construction and/or land use [12]. The interfacial evaporation has an ultra-fast response to sunlight and is endowed with a much higher systematic thermal efficiency [13,14]. Furthermore, the technique can be easily applied by floating an absorber sheet on the water surface without complex pressure control or other bulky infrastructure. Owing to all these advantages, scientists have made great efforts to develop the interfacial solar-driven evaporation.

To yield a remarkable photothermal performance, the development of interfacial evaporation structure should center around the following four key factors. (1) The ideal solar absorber should possess outstanding absorption in the range of visible and near-infrared regions to convert the solar radiation into heat to be used for water vapor generation [15–18]; (2) It is crucial for the interfacial evaporation to feature a low thermal conductivity, thereby reducing the heat loss from the absorber to the bulk water and localizing the heat at the air/water evaporative interface [19–21]; and (3) High hydrophilicity and porous framework are necessary for sufficient water transport from the bulk water to the

---
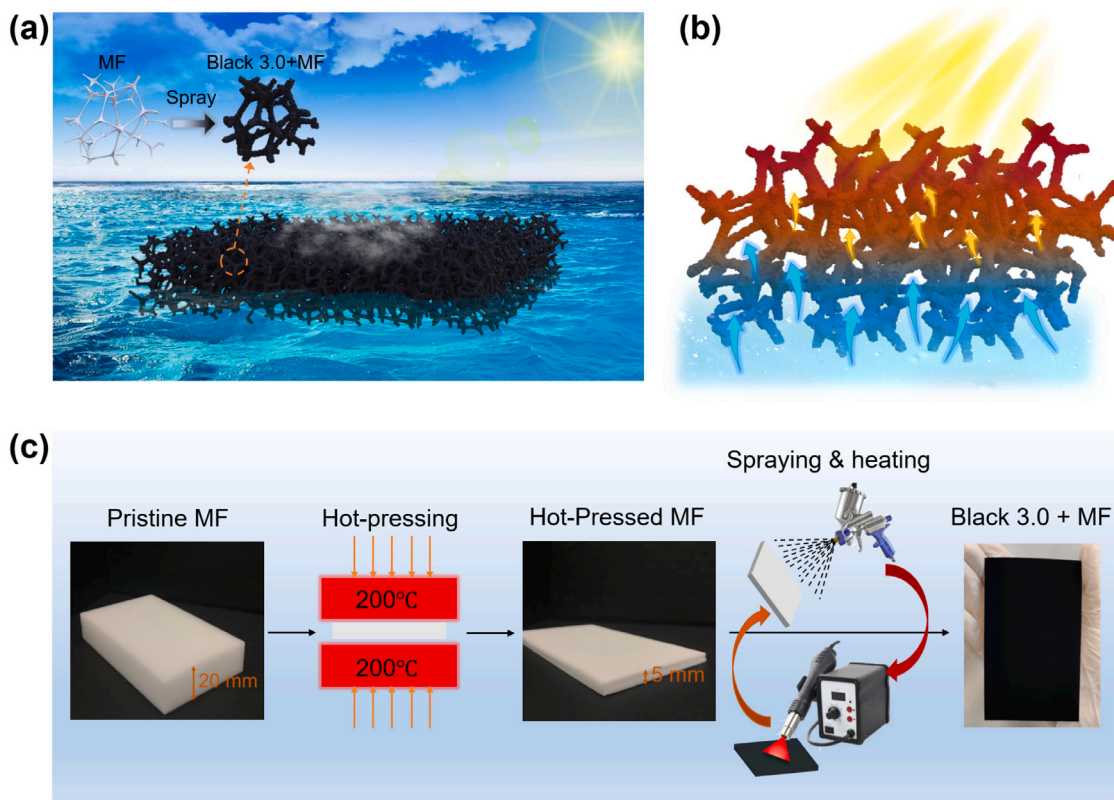
Fig. 1. Black 3.0-sprayed MF-based evaporator for solar-driven desalination. (a) Schematic illustration of solar desalination based on a solar absorber layer composed of MF, working as the supporting structure, and Black 3.0 paint, working as a photothermal material. The inset shows the structures of pristine MF and MF sprayed with a layer of Black 3.0 paint. (b) Schematic showing the mechanism of steam generation for Black 3.0 paint sprayed MF under sunlight illumination. The MF with three-dimensional interconnected porous structure is capable of pumping water for evaporation from the seawater to the upper evaporation surface ascribing to capillary force and hydrophilicity of MF (blue and yellow arrows). Under solar irradiation, Black 3.0 paint, which is attaching to the outer surface of MF, serves as a photothermal material of the solar absorber to harvest solar energy and heat surrounding water near the evaporation surface. Meanwhile, the MF with open pore structure allows vapor generated on the evaporation surface to diffuse out. (c) Schematic illustration of the fab processes of a solar absorber layer in the evaporation device.

heated area [22–25]. Basing in the concept of interfacial heating, the multilayer structure consisting of photothermal material, closed-pore thermal insulator, and external hydrophilic materials has generated much interest. The closed-pore thermal insulator serves as a real heat barrier layer and the air inside the insulator reduces heat conduction. External hydrophilic materials, wrapping or passing through the insulator foam, act as a capillary-driven pump with a one-/two-dimensional water path. By and large, this multilayered evaporation structure has become a popular way to further minimize heat conduction losses and improve energy conversion efficiency. However, considering the application in real life, especially for implementation in some underdeveloped areas with weak industries, it is still challenging for affordable and scalable deployment of solar-driven steam generators, which is hindered by high-cost raw materials, elaborate technologies, high-associated cost, and time-consuming fabrication methods. Therefore, under the premise of ensuring evaporation performance, a strategy that employs easily accessible materials, cost-efficient processing techniques, and easy-to-fabricate methods is more promising and practical for large-scale both industrial and residential applications.

With the aim to further explore materials with high evaporation performance and feasible fabrication methods for desalination, we have applied the blackest paint, called Black 3.0 paint, to the floating interfacial solar-driven evaporation device serving as the photothermal conversion material combined with a sheet of melamine foam (MF) by spraying method (Fig. 1(a)). Herein, a sheet of hot-pressed MF plays an ideal elastic skeleton material sprayed with Black 3.0 paint, serving on top as a perfect solar absorber to efficiently absorb and convert the solar radiation into thermal energy. simultaneously, water is continuously transported to the evaporation surface via the strong capillary force

resulting from three-dimensional interconnected porous structure of MF (Fig. 1(b)). To further improve evaporation performance and obtain a high solar-thermal energy conversion efficiency, the widely adopted three-layer evaporation device with a two-dimensional water path with super water absorbing capacity and an insulation foam to localize thermal energy is applied to reduce the direct contact area between MF and bulk water. This evaporation device is made from the commercially available and low-cost materials: solar absorber uses a sheet of hot-pressed MF combined with Black 3.0 paint; two-dimensional water path is provided by the highly absorbent cotton wipe, and thermal insulator uses the polyvinyl chloride (PVC) foam. Under one sun illumination, this evaporation device yields an excellent evaporation rate of freshwater as high as 2.48 kg m^{-2} h^{-1}. This evaporation device exhibits relative high performance with operability and durability, which can be regarded as one of the indispensable choices for the large-scale solar-driven evaporation process.

2. Experimental section

2.1. Materials

The commercial MF is purchased from South Street Designs company (UPC: 089902974060) with the dimension of 10 cm × 6 cm × 2 cm. Black 3.0 paint is purchased on the Culture Hustle. Cotton wipe is in the size of 0.2 m × 0.2 m supplied by Webril. The PVC foam insulator sheet is purchased from the McMaster-Carr with the dimension of 813 mm × 1219 mm × 13 mm. NaCl (99.0%) is purchased from Sigma-Aldrich.

2.2. Sample fabrication

Solar absorber layer is fabricated as follows: pristine MF (10 cm × 6 cm × 2 cm) is thoroughly washed several times with ethanol and deionized (DI) water and then put in an oven kept at 60 °C in preparation for the hot-pressing treatment. After it is totally dried, the MF is pressed at 200 °C for 6 min with a compression ratio of 4, which is the height ratio of pristine MF to hot-pressed one. Serving as the skeleton of the absorber, hot-pressed MF is cut into the desired shape with a thickness of about 1 mm. Black 3.0 paint is thinned with DI water under vigorous stirring until obtain a black homogeneous mixture. The mass ratio of DI water to Black 3.0 paint is kept in the range of 0.35–0.4 in the dilution process. Subsequently, the diluted Black 3.0 paint is sprayed onto the MF sheet by a touch-up spray gun (Paasche Airbrush, USA) with a 0.8 mm spray head at the pressure of 70 psi. The distance between the spray head and the MF sheet is about 25 cm. And then dry it completely with the hot air blower (Yihua Electronic Equipment Co., Ltd, Guangzhou, China) at a temperature of 190 °C for 5 min. It is worth noting that this drying time is suitable for the specific dimensions of the sample in this work.

A piece of PVC foam (47 mm in diameter and 13 mm in thickness) is utilized as the thermal insulator. Webril pure cotton wipe is cut into a 47 mm circle with four extended strips of 30 mm in width and 20 mm in length. The hydrophilic cotton wipe is wrapped around the PVC foam, and the four strips of it are soaked in the bulk water ensuring that water can reach the upper circular area due to capillary force. Then, the MF sheet sprayed with Black 3.0 paint is placed over the circular area of the cotton wipe.

2.3. Solar steam generation experiments

The steam generation experiments in the lab are carried out under a solar simulator (Newport, 94081 A, class ABB) which supplies solar flux of 1 kW m^{-2} with an optical filter for the standard AM 1.5 G spectrum. DI water and seawater (3.5 wt% NaCl solution) are prepared at the same initial temperature of 21 °C and placed in the 100 ml beakers with a mouth diameter of 50 mm, respectively. The steam generation device is floated on the solution surface and the mass of water is accurately monitored by an electric balance (RADWAG, PS 1000.X2.NTEP) which is connected to a computer for recording the real-time mass change. The real-time temperature is monitored by an infrared radiation camera (FLIR, A655sc) .

2.4. Materials characterizations

The reflectance spectra (0.3 μm–2.5 μm) are measured by a Jasco V770 spectrophotometer equipped with a Jasco ISN-923 integrating sphere with a fixed angle of 6°. The FTIR transmittance spectra (2.5 μm–20 μm) are measured by Jasco FTIR 6600 at a normal incident angle with reference to the background spectrum of a hydraulic pressed KBr film (20 psi). The reflectance spectra at different AOI are characterized by using wedges of different angles at the sample port of the Jasco V770 spectrophotometer. The surface morphologies of samples were characterized by an acceleration voltage of 5 kV using a Supra 25 scanning electron microscope (SEM). The thermal conductivity of the samples was characterized with the HotDisk TPS 2500 S. The contact angle was characterized by the SINDIN SDC-350 contact angle meter. The solar intensity of the solar simulator is calibrated by the TES 132 solar power meter. The salinity of collected water samples was characterized by the Extech EC400 ExStik salinity meter.

3. Results and discussion

### 3.1. Preparation and structural characterization of absorber layer

The schematic of the synthesis process of the solar absorber layer is shown in Fig. 1(c). The fabrication process is simple and scalable, which is summarized as three steps: hot-pressing, spraying, and drying. In this study, the MF with the dimension of 10 cm × 6 cm × 2 cm is selected as an elastic skeleton for immobilization of the Black 3.0 paint spray. MF is a commercially available low-cost polymer material, and its high porosity, low density, excellent hydrophilicity, and elasticity render it highly applicable for the solar steam generation devices [26,27]. In laboratory experiments, the pressed MF is cut into a 1 mm-thick circle with a diameter of 47 mm, fitting the size of the water container. The inexpensive Black 3.0 paint, commercially available as well, has gained great attention in creative art and as an superb solar photothermal material. As the blackest and most matte acrylic commercial paint, Black 3.0 paint exhibits excellent solar absorption of visible light. This paint can be easily applied via brushing or spraying onto most surfaces, such as wood, paper, canvas, and plastic. Last but not the least, the paint is light in density and very suitable to the desalination process. The diluted paint is sprayed on the pressed MF sheet using a spray gun. Considering the porous surface of the pressed MF sheet surface, it turns out that a couple of thin coating layers are better than one the thick layer. Between each coating process, drying it thoroughly with hot air is necessary at 190 °C. After completely drying, the Black 3.0 paint-coated MF sheet is rinsed in deionized (DI) water for several times to remove the residual impurities. Hereafter, keep this sheet in the oven at 60 °C for drying and then use it as a solar absorber layer in the evaporation device. The absorber layer can be easily prepared without complex process, expensive equipment, and time-consuming fabrication method, and therefore, most suitable for volume production.

Fig. 2(a) and (b) are the SEM images of top view and side view of the pristine MF, respectively. The pristine MF keeps polygon networks with a pore size of 80 μm–160 μm and the diameter of the limb is around 7 μm on the top surface (Fig. S1). After the hot-pressing process which is acting parallel to the upper surface, While the geometric shape of the networks collapses with the reduced network size (Fig. 2(c) and (d)), it retains its porous structure with more dense distribution, enabling the transportation of water. One-layer Black 3.0 paint coating forms a discontinuous wrap along the limbs or beads locating at the interactions (Fig. 2(e) and (f)). After three-layer paint coating, the MF turns completely dark. The paint forms a complete wrap fully enveloping the whole networks and causing an increase in the limb diameter from 7 μm to 35 μm (Fig. 2(g) and (h)). The fully covered MF still keeps a highly-porous structure facilitating the water transport and vapor release, which results in the high water evaporation rate.

As shown in Fig. 3(a), the solar absorber exhibits a superb absorption ranging from 95% to 99% over the broad range of wavelength from 0.3 μm to 2.5 μm, indicating that it acts as an efficient broadband solar radiation absorber, whereas the pure pressed MF shows poor absorption. Besides, this solar absorber also exhibits an angular-independent solar absorption with angle of incidence from 0° to 60°, making it work effectively during most of the daytime (Fig. 3(b) and Fig. S2). Fig. 3(c) shows the surface temperature of the absorber sheet in the air under one sun illumination for an hour. The time-dependent temperature changes and infrared (IR) images are captured by an infrared camera at room temperature, displaying the maximum temperature of the solar absorber over time. In taking the temperature measurement, the tested absorber sample is placed on a PVC foam plate to minimize the heat exchange with the base below. Upon light illumination, Black 3.0 paint attached on the outer surface of MF works as a photothermal material to absorb light and convert it into thermal energy (heat), simultaneously, the interconnected porous structure of MF with open pore is conductive to light trapping, further enhancing the light absorption. The surface temperature of the absorber sheet rises sharply to an
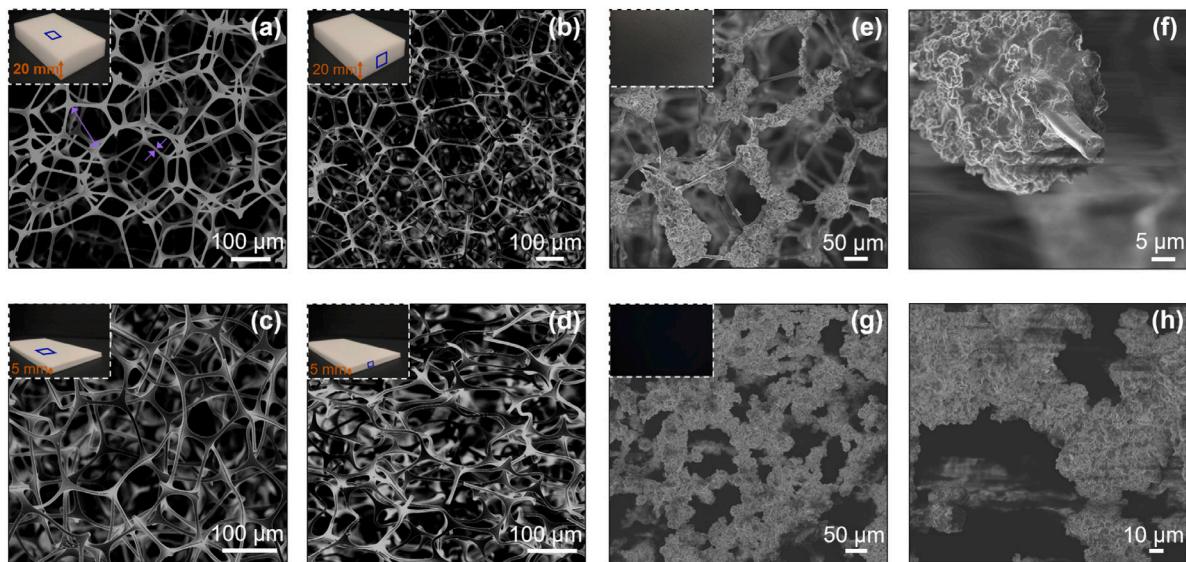
Fig. 2. Morphology of the solar absorber layer. (a–d) SEM images of top view and side view of the pristine MF and the hot-pressed MF, respectively. The inset in each SEM image shows the corresponding MF in pristine and hot-pressed states. The purple arrows indicate the pore size and the diameter of a fiber, respectively. (e,f) SEM images of MF sprayed with one layer of Black 3.0 paint with different magnifications. (g,h) SEM images of MF sprayed with three layer of Black 3.0 paint with different magnification. The insets in (e) and (h) are photographs of MF sprayed with one layer and three layer Black 3.0 paint, respectively. (For interpretation of the references to color in this figure legend, the reader is referred to the web version of this article.)
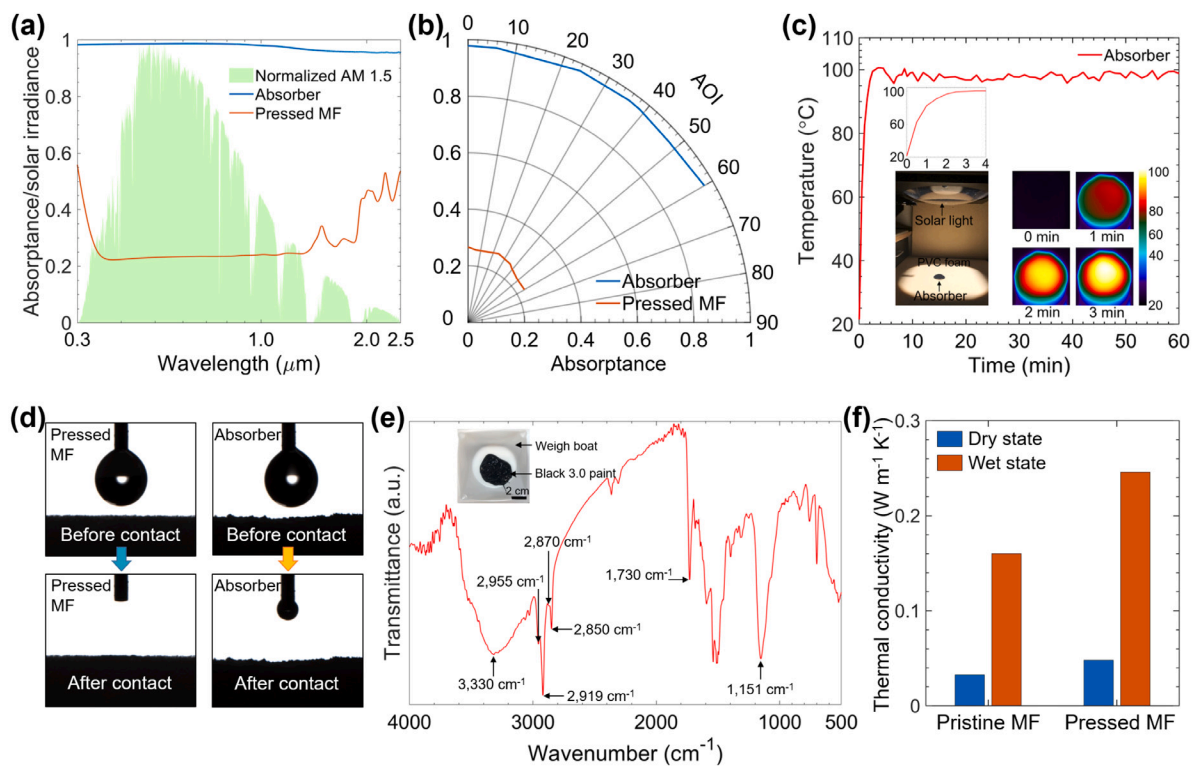
Fig. 3. (a) UV–Visible–Near-infrared absorptance of solar absorber layer, hot-pressed MF, and normalized AM 1.5 spectral irradiance. (b) The average solar absorptance of the absorber layer with various incident angles. (c) The temperature of a dry solar absorber sheet over time under one sun illumination. The insets show the corresponding setup (left) and the infrared (IR) images of the top view of solar absorber with the irradiation time of 0, 1, 2, and 3 min, respectively. (d) Dynamic contact angle measurement of hot-pressed MF and absorber layer, respectively, and both these two samples display a zero contact angle, that water droplet is instantly absorbed when it reaches the upper surface of the sample. (e) FTIR transmittance spectrum of the Black 3.0 paint hydraulic pressed with KBr powder showing corresponding wavenumber of functional groups. Inset: 5.9 g Black 3.0 paint in a weigh boat. (f) Thermal conductivities of the pristine MF and the hot-pressed MF at dry and wet states, respectively.

equilibrium temperature around 100 °C within the initial 2.5 min and then floats slightly around this temperature afterward, indicating an excellent photothermal performance of the absorber sheet. The inset of Fig. 3(c) demonstrates the changes in surface temperature more clearly in the initial 4 min.

To perform a satisfactory steam generation with continuous evaporation, water absorption capacity and transportation are required. As shown in Fig. 3(d), a dynamic water contact angle measurement is conducted for pressed MF sheet and absorber sheet, respectively, and both these two samples display a zero contact angle, that water droplet is instantly absorbed when it reaches the upper surface of the sample.

Fig. 3(e) displays the transmittance spectrum of the Black 3.0 paint which is hydraulic pressed with KBr powder showing corresponding wavenumber of functional groups. The absorption peak at 3,330 cm^{-1} is due to the −OH group, which indicates the hydrophilic property of the paint. The two peaks at 2,955 cm^{-1} and 2,870 cm^{-1} result from the asymmetric and symmetric stretching vibrations of −CH$_3$ group, respectively. The asymmetric and symmetric stretching vibrations of −CH$_2$ group cause the absorption peaks at 2,919 cm^{-1} and 2,850 cm^{-1}. The sharp absorption peak at 1,730 cm^{-1} is due to the stretching vibrations of −C=O and the stretching vibration C–O–C gives rise to the peak at 1,151 cm^{-1}. Thermal conductivities of wet pristine MF and pressed MF are 0.16 W m^{-1} K^{-1} and 0.25 W m^{-1} K^{-1}, respectively, which demonstrate big increases compared with those in the dry state (0.033 W m^{-1} K^{-1} for dry pristine MF, and 0.048 W m^{-1} K^{-1} for dry pressed MF), indicating that a large amount of water is confined into the foams, squeezing the air space in the foam (Fig. 3(f)). Even so, the wet MF possesses a lower thermal conductivity than pure water (0.598 W m^{-1} K^{-1}), which is conductive to the thermal localization limiting the heat converted from solar energy to the evaporation surface and reducing the downward conductive heat loss. After hot-pressing process, the dry MF with highly reduced air volume inside results in an increased thermal conductivity with more dense porous structure, which is leading to a stronger water absorption capability with a relatively higher value of thermal conductivity in wet state.

Tensile tests are performed to quantitatively clarify the mechanical properties of the solar absorber sheet, and tensile stress–strain curves in the dried state are obtained at room temperature before and after a 23-hour long-term desalination experiment under one sun irradiation. The tensile strength of 129.7 kPa is recorded at a large fracture strain of 35%, and no obvious damage of the mechanical properties can be observed after a long-term desalination test (Fig. S3). To evaluate the stability of the solar absorber sheet, showing the photothermal materials are capable of bonding to the MF well, the absorber layers undergo severe tests, kept in the low-temperature environment (−30 °C) for 112 h, saltwater for 128 h, boiling water (around 90 °C) for 1 h and immersed in the alkaline solution (pH ∼ 14) and acidic solution (pH ∼ 1) for 24 h in the closed bottles. After these harsh thermal and chemical stability tests, no obvious changes in the appearance are observed and their absorption spectra are basically consistent with the original one (Fig. S4–S6). In Fig. S7, the hot-pressing treatment of the MF has been experimentally confirmed to be advantageous to increase its density to effectively enhance the ability of water absorption.

3.2. Steam generation performance characterization

The steam generation performance is systematically evaluated through indoor experiments. As shown in Fig. 4(a), the evaporation device floating in a water container is placed on an electronic scale which is connected to a laptop to monitored and record the real-time mass. At the same time, the temperature distribution of evaporation surface is captured by an IR thermal camera. Solar light is supplied by a solar simulator whose intensity is calibrated to be one sun (1 kW m^{-2}). The self-floating evaporation device is composed of three layers (Fig. 4(b)). The top layer is a solar absorber layer made of a pressed MF sheet combined with Black 3.0 paint and it plays an essential role in an efficient absorption of the solar radiation. Beneath the absorber layer is a 2D water path enabled by a cotton wipe that is cut into the shape of a circle with four extended strips. The round area of the cotton wipe is kept the same as the absorber area, and the bottom edges of four strips are in direct contact with the bulk water, which decreased the contact area between the evaporation surface and the bulk water. The cotton wipe is used to transport water due to its strong capillary force and to reduce the direct contact between the bulk water and the absorber layer. Simultaneously ensuring the efficient water supply to the solar heating area and minimizing the heat dissipation to the bulk water is crucial to achieve the high-efficiency interfacial evaporation. The interlocked fibers of cotton wipe do not come apart when soaked in water for a long time, that contributes to the durability and stability of the device. In the working process, the cotton wipe pumps the bulk water towards the heating surface through the four strips around the floating foam relying on its strong capillary wicking effect. The bottom layer is the thermal insulation wrapped with the cotton water path. The thermal insulation is made from PVC foam with only closed pores which are impermeable to water, and its low thermal conductivity (∼ 0.03 W m^{-1} K^{-1}) almost reduces the downward thermal dissipation from the evaporation surface. Thanks to the low density of the thermal insulation and the simple structure of the whole device, the evaporation device can be placed on the water and move together with the waving water surface achieving self-floating for continuous operation. To further test the structure stability of this three-layer evaporation device, a series of dynamic experiments are conducted, including the shaking test, rotation test, and immersion test. The three-layer evaporation device maintains a good mechanical stability of tests without any dynamic displacement or falling off from the solar absorber sheet (Fig. S8–S10).

The surface wettability of the evaporation device also plays an important role in the steam generation process. As shown in Fig. 4(c), the evaporation device is placed in a beaker filled with DI water at the initial temperature of 21 °C, and its wetting process is recorded from the top view. It is obvious that the water immediately reaches the surface of the absorber layer from the regional edge (the enclosed areas in the blue dashed), and then the wet area quickly expands to the central area until it covers the entire evaporation surface. The surface wettability owes much to forceful hydrophilicity of the two-dimensional water path of the cotton and the porous structure of the absorber layer, which assures ample water supply to the evaporation surface.

Fig. 4(d) compares the surface temperatures of evaporation device (top row) and pure water (bottom row) upon exposure to one sun illumination. Under light illumination, the temperature of the absorber layer rises sharply to an equilibrium temperature around 49 °C, indicating good photothermal performance. In contrast, the surface temperature of pure water rises slowly under irradiation owing to the poor light harvesting efficiency, and its maximum temperature profile slopes gently from the initial temperature of 21 °C to 32 °C for an hour, while stable surface temperature with evaporation device stabilizes around 50 °C (Fig. 4(e)). For the water only experiment, the evaporation rate is measured to be 0.41 kg m^{-2} h^{-1} within the initial 1 h under one sun irradiation (Fig. 4(f)). In contrast, the evaporation rate of evaporation device with DI water reaches up to 2.48 kg m^{-2} h^{-1} under the same experimental conditions, 6.04 times higher than that of pure water, which has an outstanding performance compared with other reported works (Table S1). Most significantly, when the evaporation device floats on the 3.5 wt% NaCl solution, it sports a comparable evaporation rate of 2.32 kg m^{-2} h^{-1}, 5.65 times higher than that of pure water. The temperature changes of the bulk water during an hour desalination work are recorded. A temperature increase of 0.54 °C is obtained, yielding the conductive heat loss of 29.6 W m^{-2}. The relevant calculation is provided in Fig. S11. Photothermal efficiency, $\eta_{pt} = \dot{m}h_{fg}/Q_s$, is an important parameter to evaluate the steam generation performance, where $\dot{m}$ is the net water evaporation rate, in which the evaporation rate in the dark environment is subtracted from the measured evaporation rate under the sunlight (kg m^{-2} h^{-1}), Q_s is the power density of irradiation (kW m^{-2}), and h_{fg} is the equivalent vaporization enthalpy of water in a porous structure absorber (kJ kg^{-1}). Thus, in the laboratory experiments, the photothermal efficiency reaches 85.1%. The specific calculation process of each term in the equation of photothermal efficiency for this evaporation device is provided in Note S1 in the supporting information.

A long-term desalination experiment over 23 h, which is divided into 5 times (5 h × 3 times and 4 h × 2 times), has been conducted to test durability and stability of the evaporation device (Fig. 4(g)). After
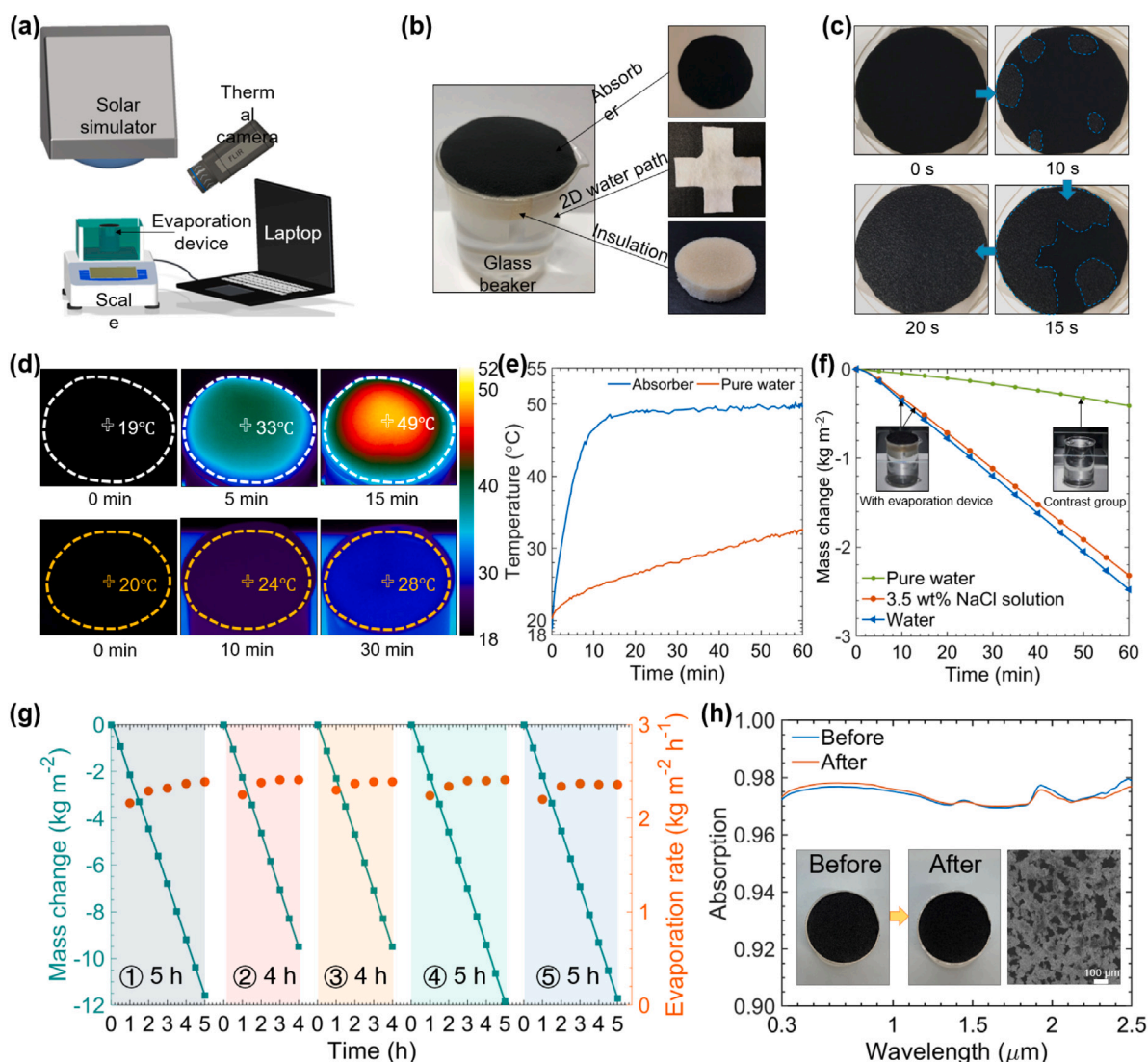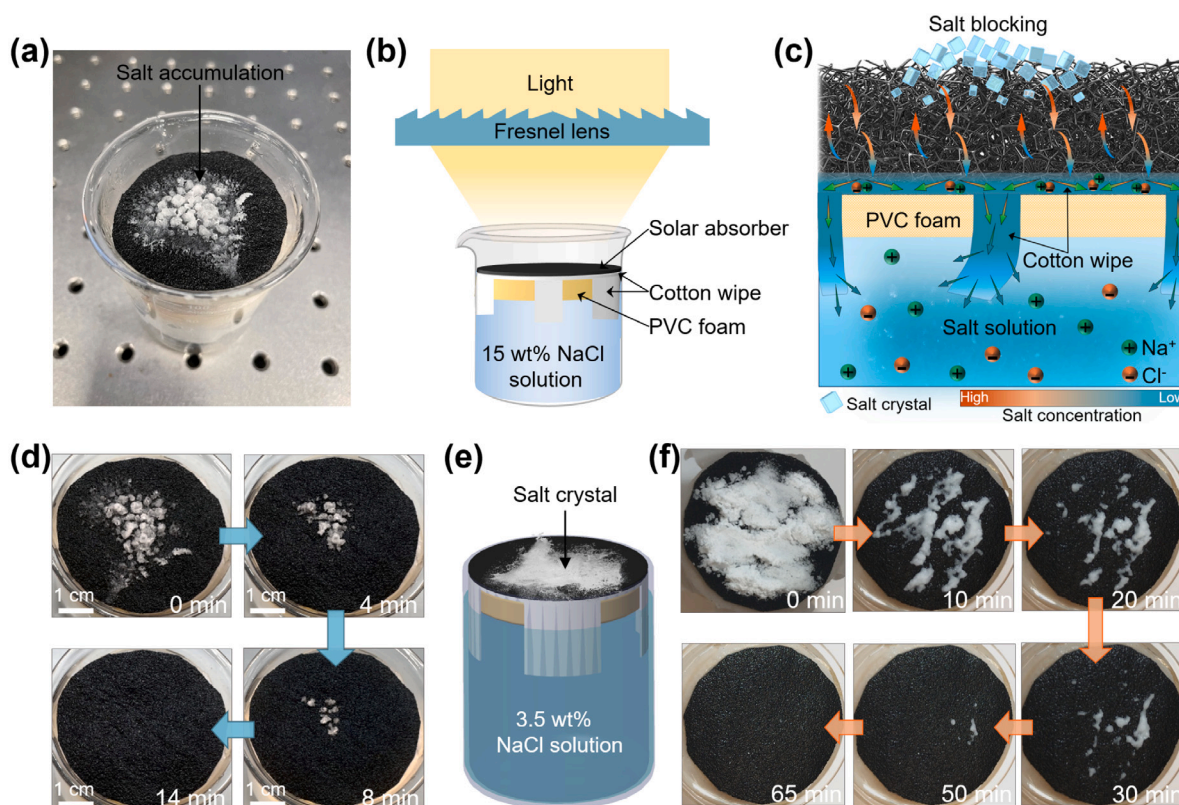
Fig. 4. Schematic illustration of the experimental setup for solar-driven steam generation tests. (b) The photograph of a evaporation device consisting of a solar absorber layer (hot-pressed MF sprayed with Black 3.0 paint), a 2D water path (cotton wipe), and an insulation layer (PVC foam). (c) Wetting process of the evaporation device placed on the surface of the water. The blue-dash enclosed regions exhibit the wetting areas. (d) IR images showing the temperature distribution of evaporation surfaces of evaporation device (top row) and water only (bottom row) when exposed to 1 sun irradiation at 0, 5, and 15 min, respectively. The white cross signs display the central temperature. (e) The central temperature of the evaporation surfaces of solar absorber layer in evaporation device and pure water, respectively. (f) Mass changes of water over time of DI water only and with the evaporation device placed at the interfaces of the DI water, and 3.5 wt% NaCl solution, respectively. Insets showing photographs of evaporation device placed in water (left) and pure water (right), respectively. (g) Mass changes and the corresponding evaporation rates in 3.5 wt% NaCl solutions with the evaporation device in a long-term stability test up to 23 h. (h) Solar absorptance spectra of the solar absorber layer in the wet state before and after the long-term desalination experiment. Inset (left) are photographs of the solar absorber layers in the wet state before and after the long-term experiment. Inset (right) is a SEM image showing that the photothermal materials (Black 3.0 paint) are well bonded to MF limbs after the long-term desalination experiment.

each period, the bulk water (3.5 wt% NaCl solution) is replaced to keep the salinity of the water supply constant at 3.5 wt%. Except for the first 10-minute preheating stage of the solar absorber surface (from room temperature to the equilibrium temperature), a linear mass change curve is observed when the evaporation device is illuminated under 1 sun for each long-term period. Obviously, these five mass change curves are almost parallel to each other, indicating the performance stability of the evaporation device. Moreover, the evaporation rate corresponding to each hour in the long-term test fluctuates in the range of 2.20–2.45 kg m^{-2} h^{-1}. For each test, the evaporation rate of the first an hour is slightly lower than the following hours due to the 10-minute preheating stage of the solar absorber surface. The absorptance spectra of the solar absorber layer before and after the long-term experiment are tested, and results are shown in Fig. 4(h). These two curves remain almost consistent, elucidating the spectrum stability of the black solar absorber layer. Meanwhile, photographs of

the solar absorber layer in the wet state before and after the long-term desalination test have no visible difference. The SEM image indicates that the photothermal materials are bonded well to the MF limbs, demonstrating the long-term stability of the solar absorber layer as well. All tests about the evaporation performance are conducted in a dark room with the dimension of 3 m × 3 m × 2.5 m. The temperature and humidity data during the long-term evaporation processes of the dark room are provided in the Fig. S12.

Avoiding salt accumulation during the evaporation process is a significant character for an evaporation device for real-life feasible implementation [28–31]. To evaluate the salt self-cleaning capability of the evaporation device, simulated salt accumulation and salt self-cleaning processes on the absorber top surface are performed. Due to the excellent water absorption ability of the evaporation device, it is hard to accumulate salt crystals on the absorber surface, therefore, a concentrated solar illumination (11 kW m^{-2}) of high intensity and a

Fig. 5. (a) Photograph showing the salt accumulation occurring at the evaporation surface with a high salinity solution and under concentrated sunlight. (b) Schematic illustration of experimental setup for salt accumulation. (c) Schematic showing the mechanism of the salt self-cleaning capability of the evaporation device. (d) Photographs of a salt self-cleaning progress of the evaporation device with accumulated salt placing in 3.5 wt% NaCl solution under ambient condition. (e) Schematic illustration of the salt self-cleaning property setup for the evaporation device with extra added salt. The evaporation device is placed in a beaker filled with a 3.5 wt% NaCl solution, and NaCl is originally stacked on the top surface of the absorber. (f) Photographs showing the progress of salt gradually dissolving over time.

high-salinity water supply (15 wt% NaCl solution) to expedite the salt accumulation. Fig. 5(a) depicts the accumulated salt crystals at the center of the evaporation surface. The experimental setup consists of a solar simulator to generate stable collimated light and a Fresnel lens to concentrated light into a high flux (Fig. 5(b)). The distance between the top surface of the absorber and the Fresnel lens is well adjusted to stabilize at 11 kW m^{-2}. The salt concentration at the top region of the absorber increases dramatically due to the fast evaporation and gradually approaches saturation. As evaporation continues, salt crystals slowly accumulated on the top surface of the absorber. After 35 min, salt crystals accumulate on the top surface of the black absorber layer while the water salinity inside the solar absorber reaches the saturation point (Fig. S13). Then, the solar simulator is shut down, and the evaporation device with massive self-accumulated salt crystals is placed in a water container filled with a 3.5 wt% NaCl solution to test its salt self-cleaning capacity. The mechanism of salt self-cleaning process of the evaporation device is as follows (Fig. 5(c)). Without ultrahigh solar intensity input, strong evaporation is extinguished. As the evaporation rate is lower than the water pumping rate, there is excess water to help to dissolve the accumulated salt crystals, keeping the solar absorber layer at an unsaturated state. The salt concentration gradient from the upper region of the black absorber layer to its lower region drives the salt ions down to the underlying bulk water through diffusion pathways. The water path of the absorber and the cotton wipe with interconnected porous structures provides a drainage way for salt ions. The micro-sized porous structures of the cotton wipe build up a bridge from the absorber and the underlying 3.5 wt% NaCl solution, which eventually facilitates the continuously salt self-cleaning process [32–40]. The salt self-cleaning process of the evaporation device is monitored and shown in Fig. 5(d). Most of the salt crystals dissolve within the first 4 min, elucidating the rapid salt self-cleaning

capability of the evaporation device. All the accumulated salt crystals dissolve back to the bulk water within 14 min. The amount of the accumulated salt under high solar flux is relatively small compared with extra added salt crystals. Fig. 5(e) shows the setup for salt self-cleaning ability test of evaporation device with extra added salt on the evaporation surface. In this test, the evaporation device with a diameter of 47 mm floated in a beaker filled with a 3.5 wt% NaCl solution with an initial temperature of 21 °C, and 1.7 g of additional salt crystals are placed directly on the top of the absorber surface. Upon contact with water, the solid NaCl on evaporation surface starts to dissolve due to the movement and exchange of solution inside the absorber layer and water path of the cotton wipe connecting evaporation surface with the bulk water below the insulation. After approximately 65 min, the evaporation device fully rejects the extra added salt, indicating its good salt rejection ability (Fig. 5(f)).

3.3. Field test

We have performed field test of this evaporation device to demonstrate the feasibility of scalable production of freshwater. We construct a prototype of the evaporation system with a condensation chamber and an evaporation device of a large area of the absorber (24 cm × 24 cm) inside, as shown in Fig. 6(a) and Fig. S14. The condensation chamber made of polymethyl methacrylate (PMMA) board surrounds the entire evaporation device to capture condensate of the evaporated steam. According to the transmission spectrum of the PMMA board, shown in Fig. S15, the condensation structure is well transparent in the solar spectrum to allow the solar irradiance to reach the evaporation device, while it is opaque in the mid-infrared region to confine the infrared emission of the evaporation device inside the chamber to contribute to maintaining a relatively higher evaporation temperature. As
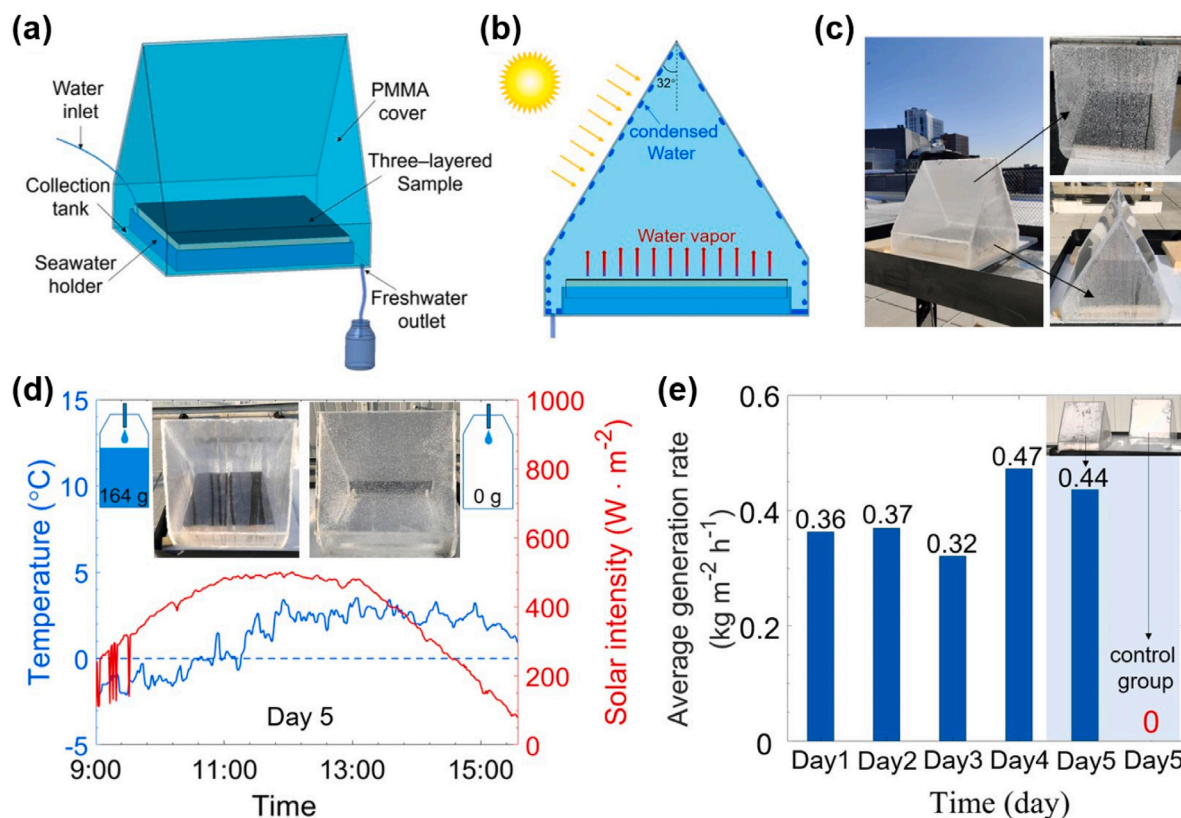
Fig. 6. Rooftop experiments with the evaporation system under natural sunlight in January 2020 in Boston, MA, USA. (a) 3D model of the evaporation system with a PMMA condensation cover in the dimension of 30 cm × 30 cm for desalination. (b) Schematic illustration of the solar desalination system. (c) Photographs of the evaporation system placed on a utility cart (left) and the dense condensed water droplets on the interior surface of the condensation cover and sidewall (right) during the experiment. (d) The contrast experiment with an evaporation device (left inset) and without (right inset) on the Day 5. The blue and red curves show the change of ambient temperature (left y-axis) and the solar intensity (right y-axis), respectively. Two bottles insets show the weight of the collected water from the contrast experiment. (e) The averaged outdoor steam generation rates of the 3.5 wt% NaCl solutions for 5 days in January 2020.

shown in Fig. 6(b), The condensed water droplets fall to the collection tank and eventually flow to a chemical storage bottle. The tilted angle of the condensation cover in the dimension of 30 cm × 30 cm is fixed to be 32° considering the latitude of Boston city, allowing the solar flux to reach the evaporator without refraction. The photograph of Fig. 6(c) shows the prototype is placed on the polystyrene foam with a low thermal conductivity to reduce the thermal flux between the bottom of the prototype and the utility cart, and the condensed water is observed on the condensation cover (Fig. S16). It has been confirmed that the sodium concentration of the desalinated water is 5 mg l^{-1}, that is much lower than the standard of the drinkable water specified by the World Health Organization (WHO) [41]. The validated prototype is tested on the roof of Snell Engineering Center at Northeastern University, Boston, MA, USA, and water collections are measured over 5 days in January 2020. The specific experiment dates, instantaneous incident sunlight, ambient temperature, wind speed, and humidity are recorded and provided in the supplementary materials. The 3.5 wt% NaCl solution, which simulates the average salinity of seawater all over the world, is used during the field test and the seawater holder is filled up through the water injection tube after the daily use.

The average evaporation rate of drinkable freshwater, shown in Fig. 6(e), varies from 0.32 kg m^{-2} h^{-1} to 0.47 kg m^{-2} h^{-1} under various solar intensity and ambient temperature. The experiment data and detailed weather condition data are provided in Fig. S17 and S18. To demonstrate the promising solar steam generation ability of this evaporation system, the prototype, and the control group, the same condensation chamber without a evaporation device inside is conducted for a contrast experiment on day 5 (Fig. 6(d)). At the end of the experiment, 164 g of water is collected from the prototype,

while the control group collects nearly zero water in the same-day operation. In the rooftop experiments, it is well noted that the weight of collected freshwater refers to the weight of water in the chemical storage bottle, not exactly the weight of condensed water produced. The inset of Fig. 6(d) shows the end state of the contrast experiment. Obviously in the control group, dense condensed water droplets can be observed on the cover without forming the water dripping flow (Fig. S19). In day 4, the daily condensate rate (2.83 kg m^{-2} d^{-1}) in winter produced from the evaporation device of the area of 0.0576 m^{-2}. which proves a reliable and scalable production of freshwater using our design in four seasons.

4. Conclusions

In summary, we have demonstrated a facile and high-performance evaporation device based on a novel commercial Black 3.0 paint, which is applied for the first time to the solar steam generation as a promising candidate for the photothermal materials. All commercially available materials and easy-to-fabricate processes render the design of this evaporation device a practical technique for people to achieve efficient freshwater yields in an affordable, robust, and scalable manner. Black 3.0 paint sprayed on a sheet of MF serves as the top solar absorber layer that can widely absorb the solar radiation and efficiently convert it into heat. The absorber layer which is placed on a PVC foam plane under one sun irradiation shows a significant temperature gradient and reaches up to 100 °C of equilibrium temperature. The absorber is shown to sport strong thermal and chemical stability under harsh environment, and it exhibits a remarkable salt rejection ability. All these performance contribute to the long-term durable steam generation process. In the laboratory experiments, enabled by the assistance

of the low thermal conductivity PVC foam to reduce the heat loss and the cotton wipe to provide sufficient water through a 2D water path to the heating region, the evaporation device has reached a striking steam generation rate of 2.48 kg m^{-2} h^{-1}, 6.04 times higher than the natural evaporation, and a photothermal efficiency of 85.1% under one sun irradiation at the room temperature, surpassing most of the reported work. Even in the rooftop experiment during a cloudy winter day in Boston, MA with the maximum environment temperature of 4 °C, 2.83 kg m^{-2} d^{-1} of water can be collected. This simple, and easy to manufacture evaporation device is highly beneficial to large scale water desalination and purification applications.

CRediT authorship contribution statement

Xiaojie Liu: Methodology, Experimentation, Validation, Analysis, Writing – original draft. **Yanpei Tian:** Methodology, Experimentation, Validation, Analysis, Writing – original draft. **Fangqi Chen:** Conceptualization, Validation. **Ralph Ahlgren:** Discussion, Methodology. **Yiting Zheng:** Discussion, Investigation. **Ming Su:** Discussion, Investigation. **Gang Xiao:** Discussion, Investigation. **Yi Zheng:** Conceptualization, Supervision, Project administration, Writing – review & editing, Funding acquisition.

Declaration of competing interest

The authors declare that they have no known competing financial interests or personal relationships that could have appeared to influence the work reported in this paper.

Acknowledgment

Appendix A. Supplementary data

Supplementary material related to this article can be found online at https://doi.org/10.1016/j.solmat.2021.111436.

References

[1] M.M. Mekonnen, A.Y. Hoekstra, Four billion people facing severe water scarcity, Sci. Adv. 2 (2) (2016) e1500323.

[2] J.H. Reif, W. Alhalabi, Solar-thermal powered desalination: Its significant challenges and potential, Renew. Sustain. Energy Rev. 48 (2015) 152–165.

[3] S.A. Kalogirou, Solar thermal collectors and applications, Prog. Energy Combust. Sci. 30 (3) (2004) 231–295.

[4] L. Zhang, Z. Xu, L. Zhao, B. Bhatia, Y. Zhong, S. Gong, E.N. Wang, Passive, high-efficiency thermally-localized solar desalination, Energy Environ. Sci. 14 (4) (2021) 1771–1793.

[5] S.M. Pourkiaei, M.H. Ahmadi, M. Ghazvini, S. Moosavi, F. Pourfayaz, R. Kumar, L. Chen, Status of direct and indirect solar desalination methods: comprehensive review, Eur. Phys. J. Plus 136 (5) (2021) 1–36.

[6] F. Alnaimat, M. Ziauddin, B. Mathew, A review of recent advances in humidification and dehumidification desalination technologies using solar energy, Desalination 499 (2021) 114860.

[7] P. Tao, G. Ni, C. Song, W. Shang, J. Wu, J. Zhu, G. Chen, T. Deng, Solar-driven interfacial evaporation, Nat. Energy 3 (12) (2018) 1031–1041.

[8] G. Ni, N. Miljkovic, H. Ghasemi, X. Huang, S.V. Boriskina, C.-T. Lin, J. Wang, Y. Xu, M.M. Rahman, T. Zhang, et al., Volumetric solar heating of nanofluids for direct vapor generation, Nano Energy 17 (2015) 290–301.

[9] J. Zhou, Y. Gu, P. Liu, P. Wang, L. Miao, J. Liu, A. Wei, X. Mu, J. Li, J. Zhu, Development and evolution of the system structure for highly efficient solar steam generation from zero to three dimensions, Adv. Funct. Mater. 29 (50) (2019) 1903255.

[10] I. Ibrahim, V. Bhoopal, D.H. Seo, M. Afsari, H.K. Shon, L.D. Tijing, Biomass-based photothermal materials for interfacial solar steam generation: A review, Mater. Today Energy (2021) 100716.

[11] S. Cao, P. Rathi, X. Wu, D. Ghim, Y.-S. Jun, S. Singamaneni, Cellulose nanomaterials in interfacial evaporators for desalination: A "natural" choice, Adv. Mater. 33 (28) (2021) 2000922.

[12] Y. Zeng, J. Yao, B.A. Horri, K. Wang, Y. Wu, D. Li, H. Wang, Solar evaporation enhancement using floating light-absorbing magnetic particles, Energy Environ. Sci. 4 (10) (2011) 4074–4078.

[13] P. Wang, Emerging investigator series: the rise of nano-enabled photothermal materials for water evaporation and clean water production by sunlight, Environ. Sci. Nano 5 (5) (2018) 1078–1089.

[14] Z. Wang, Y. Liu, P. Tao, Q. Shen, N. Yi, F. Zhang, Q. Liu, C. Song, D. Zhang, W. Shang, et al., Bio-inspired evaporation through plasmonic film of nanoparticles at the air–water interface, Small 10 (16) (2014) 3234–3239.

[15] M. Kim, K. Yang, Y.S. Kim, J.C. Won, P. Kang, Y.H. Kim, B.G. Kim, Laser-induced photothermal generation of flexible and salt-resistant monolithic bilayer membranes for efficient solar desalination, Carbon 164 (2020) 349–356.

[16] Y. Zou, P. Yang, L. Yang, N. Li, G. Duan, X. Liu, Y. Li, Boosting solar steam generation by photothermal enhanced polydopamine/wood composites, Polymer 217 (2021) 123464.

[17] R. Zhu, M. Liu, Y. Hou, D. Wang, L. Zhang, D. Wang, S. Fu, Mussel-inspired photothermal synergetic system for clean water production using full-spectrum solar energy, Chem. Eng. J. 423 (2021) 129099.

[18] G. Chen, Z. Jiang, A. Li, Z. Ma, X. Chen, H. Song, Cu-based MOF-derived porous carbon with highly efficient photothermal conversion performance for solar steam evaporation, J. Mater. Chem. A (2021).

[19] T. Gao, X. Wu, Y. Wang, G. Owens, H. Xu, A hollow and compressible 3D photothermal evaporator for highly efficient solar steam generation without energy loss, Solar RRL 5 (5) (2021) 2100053.

[20] K. Nabeela, M.N. Thorat, S.N. Backer, A.M. Ramachandran, R.T. Thomas, G. Preethikumar, A.P. Mohamed, A. Asok, S.G. Dastager, S. Pillai, Hydrophilic 3D interconnected network of bacterial nanocellulose/black titania photothermal foams as an efficient interfacial solar evaporator, ACS Appl. Bio Mater. 4 (5) (2021) 4373–4383.

[21] A. Mnoyan, M. Choi, D.H. Kim, B.-J. Ku, H. Kim, K.J. Lee, A.S. Yasin, S. Nam, K. Lee, Cheap, facile, and upscalable activated carbon-based photothermal layers for solar steam generation, RSC Adv. 10 (69) (2020) 42432–42440.

[22] C.-R. Zhang, W.-R. Cui, C.-P. Niu, S.-M. Yi, R.-P. Liang, J.-X. Qi, X.-J. Chen, W. Jiang, L. Zhang, J.-D. Qiu, rGO-based covalent organic framework hydrogel for synergistically enhance uranium capture capacity through photothermal desalination, Chem. Eng. J. (2021) 131178.

[23] D.P. Storer, J.L. Phelps, X. Wu, G. Owens, N.I. Khan, H. Xu, Graphene and rice-straw-fiber-based 3D photothermal aerogels for highly efficient solar evaporation, ACS Appl. Mater. Interfaces 12 (13) (2020) 15279–15287.

[24] H. Wang, R. Zhang, D. Yuan, S. Xu, L. Wang, Gas foaming guided fabrication of 3D porous plasmonic nanoplatform with broadband absorption, tunable shape, excellent stability, and high photothermal efficiency for solar water purification, Adv. Funct. Mater. 30 (46) (2020) 2003995.

[25] J. He, Y. Fan, C. Xiao, F. Liu, H. Sun, Z. Zhu, W. Liang, A. Li, Enhanced solar steam generation of hydrogel composite with aligned channel and shape memory behavior, Compos. Sci. Technol. 204 (2021) 108633.

[26] X. Lin, J. Chen, Z. Yuan, M. Yang, G. Chen, D. Yu, M. Zhang, W. Hong, X. Chen, Integrative solar absorbers for highly efficient solar steam generation, J. Mater. Chem. A 6 (11) (2018) 4642–4648.

[27] C. Li, D. Jiang, B. Huo, M. Ding, C. Huang, D. Jia, H. Li, C.-Y. Liu, J. Liu, Scalable and robust bilayer polymer foams for highly efficient and stable solar desalination, Nano Energy 60 (2019) 841–849.

[28] G. Ni, S.H. Zandavi, S.M. Javid, S.V. Boriskina, T.A. Cooper, G. Chen, A salt-rejecting floating solar still for low-cost desalination, Energy Environ. Sci. 11 (6) (2018) 1510–1519.

[29] Y. Kuang, C. Chen, S. He, E.M. Hitz, Y. Wang, W. Gan, R. Mi, L. Hu, A high-performance self-regenerating solar evaporator for continuous water desalination, Adv. Mater. 31 (23) (2019) 1900498.

[30] X. Dong, Y. Si, C. Chen, B. Ding, H. Deng, Reed leaves inspired silica nanofibrous aerogels with parallel-arranged vessels for salt-resistant solar desalination, ACS Nano (2021).

[31] F. Wang, Z. Hu, Y. Fan, W. Bai, S. Wu, H. Sun, Z. Zhu, W. Liang, A. Li, Salt-rejection solar absorbers based on porous ionic polymers nanowires for desalination, Macromol. Rapid Commun. 42 (4) (2021) 2000536.

[32] J. He, Z. Zhang, C. Xiao, F. Liu, H. Sun, Z. Zhu, W. Liang, A. Li, High-performance salt-rejecting and cost-effective superhydrophilic porous monolithic polymer foam for solar steam generation, ACS Appl. Mater. Interfaces 12 (14) (2020) 16308–16318.

[33] S. Wang, Y. Fan, F. Wang, Y. Su, X. Zhou, Z. Zhu, H. Sun, W. Liang, A. Li, Potentially scalable fabrication of salt-rejection evaporator based on electrogenerated polypyrrole-coated nickel foam for efficient solar steam generation, Desalination 505 (2021) 114982.

[34] J. Li, X. Zhou, P. Mu, F. Wang, H. Sun, Z. Zhu, J. Zhang, W. Li, A. Li, Ultralight biomass porous foam with aligned hierarchical channels as salt-resistant solar steam generators, ACS Appl. Mater. Interfaces 12 (1) (2019) 798–806.

[35] K. Liu, W. Zhang, H. Cheng, L. Luo, B. Wang, Z. Mao, X. Sui, X. Feng, A nature-inspired monolithic integrated cellulose aerogel-based evaporator for efficient solar desalination, ACS Appl. Mater. Interfaces 13 (8) (2021) 10612–10622.

[36] K. Xu, C. Wang, Z. Li, S. Wu, J. Wang, Salt mitigation strategies of solar-driven interfacial desalination, Adv. Funct. Mater. 31 (8) (2021) 2007855.

[37] G. Liu, T. Chen, J. Xu, G. Yao, J. Xie, Y. Cheng, Z. Miao, K. Wang, Salt-rejecting solar interfacial evaporation, Cell Rep. Phys. Sci. 2 (1) (2021) 100310.

[38] Y. Tian, X. Liu, Z. Wang, A. Caratenuto, F. Chen, Y. Wan, Y. Zheng, Carbonized cattle manure-based photothermal evaporator with hierarchically bimodal pores for solar desalination in high-salinity brines, Desalination 520 (2021) 115345.

[39] Q. Huang, C. Du, C. Guo, C. Huang, X. Wang, A high-efficiency salt-rejecting solar evaporator with optimized porous structure for continuous solar desalination, Appl. Therm. Eng. 187 (2021) 116515.

[40] Y. Zou, J. Zhao, J. Zhu, X. Guo, P. Chen, G. Duan, X. Liu, Y. Li, A mussel-inspired polydopamine-filled cellulose aerogel for solar-enabled water remediation, ACS Appl. Mater. Interfaces 13 (6) (2021) 7617–7624.

[41] W.H. Organization, et al., Safe Drinking-Water from Desalination, Technical Report, World Health Organization, 2011.